JOURNAL OF AIRCRAFT
Vol. 42, No. 2, March–April 2005

# Airfoil Pitch-and-Plunge Bifurcation Behavior with Fourier Chaos Expansions

D. R. Millman* and P. I. King†
*Air Force Institute of Technology, Wright–Patterson Air Force Base, Ohio 45433*
and
P. S. Beran‡
*U.S. Air Force Research Laboratory, Wright–Patterson Air Force Base, Ohio 45433*

**A stochastic projection method is employed to obtain the probability distribution of pitch angle of an airfoil in pitch and plunge subject to probabilistic uncertainty in both the initial pitch angle and the cubic spring coefficient of the restoring pitch force. Historically, the selected basis for the stochastic projection method has been orthogonal polynomials, referred to as the polynomial chaos. Such polynomials, however, result in unacceptable computational expense for applications involving oscillatory motion, and a new basis, the Fourier chaos, is introduced for computing limit-cycle oscillations. Unlike the polynomial chaos expansions, which cannot predict limit-cycle oscillations, the Fourier chaos expansions predict both subcritical and supercritical responses even with low-order expansions and high-order nonlinearities. Bifurcation diagrams generated with this new approximate method compare well to Monte Carlo simulations.**

## Introduction

AN unsteady fluid-structure interaction can cause the loss of dynamic stability at some critical dynamic pressure and result in an unbounded time periodic instability.[1] Nonlinear aerodynamics (e.g., caused by transient shocks or boundary-layer separation) and nonlinear structural responses (e.g., caused by damping) can counteract the growth of unstable modes and cause the dynamic response to stabilize to a limit-cycle oscillation (LCO).[2−6] Such LCOs have occurred in flight, where several fighter aircraft with external stores have exhibited LCO under certain conditions.[2] The LCO is characterized by antisymmetric motion of the wing and can lead to fatigue failure.

For structures susceptible to LCO, an increasing dynamic pressure will reach a critical value, the Hopf bifurcation point, at which LCO begins. Figure 1 shows two possible outcomes for increased dynamic pressure above the Hopf bifurcation point: a small-amplitude LCO and a large-amplitude LCO. On the small-amplitude LCO branch, referred to as the supercritical response, the amplitude of the LCO increases slowly with increasing dynamic pressure. If the dynamic pressure is decreased from above the Hopf bifurcation point to below the Hopf bifurcation point, the structure will cease LCO. The second possibility when transitioning through the Hopf bifurcation point is a jump to the large-amplitude LCO or subcritical response. For this case, LCO will not cease until dynamic pressure is decreased to a new critical value (hysteretic behavior), defined as the turning-point bifurcation.[7] Wind-tunnel investigations[4] on a high-aspect-ratio wing at transonic speeds have verified the existence of large- and small-amplitude LCOs and the Hopf bifurcation point. The hysteretic behavior associated with the large-amplitude LCO has been seen in flight test.[2] To compute the supercritical and subcritical dynamic response of an aeroelastic system, one employs a time integration of the discrete aeroelastic equations.[3] The equations contain parameters whose values are user selected and which can vary over a wide range. Only certain values or ranges of parameters, however, result in Hopf bifurcations. One can search for the bifurcation using slope techniques with small variations in input parameters, but the search can be prolonged as a result of the strong and nonlinear effects of such small variations.[8] An alternative approach is to assign probabilistic distributions to certain input variables and perform Monte Carlo simulation (MCS) to obtain probability distribution functions (PDFs) of supercritical and subcritical responses. These PDFs can be used to estimate the bifurcation diagrams and estimate probability of failure. A full-scale, high-fidelity MCS solution can be prohibitive in terms of CPU time, however, and so low-fidelity modeling of the aerodynamics and structure is usually employed, but at a cost in predictive accuracy of the flow field and structural response. Variational techniques[9] can reduce the effort of MCS within a prescribed confidence level, but the number of realizations required to identify bifurcations such as those in Fig. 1 can still be quite large.[8]

Approximate methods have been used with probabilistic inputs, such as the first-order and second-order reliability methods (FORM and SORM).[10,11] Classically, FORM and SORM have been used to estimate the most probable point of failure through response surface modeling.[12] With these two methods, the required solution variable expansions are local and not well suited to highly nonlinear problems. These methods also fail to predict stationary bifurcations.[12] An approximate method suited to nonlinear systems is reduced-order modeling (ROM), which represents a full-order model with an optimal basis, in the mean square sense, through a Karhunen–Loeve expansion (KLE).[13−16] ROM has the advantage that it can be efficiently tuned to capture flow physics at a high fidelity. Monte Carlo simulations are far more efficient on a reduced-order model than on the full-order system, and these simulations can estimate responses about the mean that are useful in a multidisciplinary design.[13] However, the variations about the mean must be small in order for the ROM to remain valid.

The stochastic projection method[12,17−22] also includes the use of an output variable expansion, but, unlike a KLE, does not require knowledge of the form of the response. In the stochastic projection method, input parameters are assigned a probability distribution.[10] Realizations (solutions) are obtained based on these distributions and combined into PDFs of the response. The process incorporates

Presented as Paper 2003-3515 at the AIAA 21st Applied Aerodynamics Conference, Orlando, FL, 23–26 June 2003; received 1 October 2003; revision received 17 May 2004; accepted for publication 20 May 2004. 

*Ph.D. Candidate and Major, USAF, Department of Aeronautics and Astronautics. Senior Member AIAA.
†Professor, Department of Aeronautics and Astronautics. Senior Member AIAA.
‡Senior Research Aerospace Engineer, AFRL/VASD. Associate Fellow AIAA.

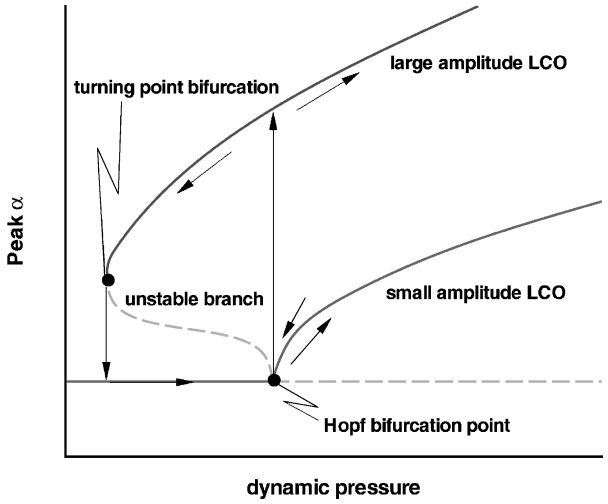


**Fig. 1 Qualitative bifurcation diagram.**

a basis orthogonal to the input uncertainty distribution, and the coefficients of the expansion are computed as part of the time integration. The expansion of a response $\alpha(t, \boldsymbol{\xi})$ takes the form[17]

$$\alpha(t, \boldsymbol{\xi}) = \sum_{i=0}^{P(p,d)} \alpha_i(t)\Psi_i(\boldsymbol{\xi}) \tag{1}$$

where

$$P(p, d) = \sum_{s=1}^{p} \frac{1}{s!} \prod_{r=0}^{s-1} (d + r) \tag{2}$$

The order of the expansion is $p$, and the number of input uncertainties, that is, the dimension of $\boldsymbol{\xi}$, is $d$.

If a Gaussian normal distribution is chosen for the input parameters, the distribution is given in terms of a zero mean, unit variance stochastic vector $\boldsymbol{\xi}$. The weight function for the Gaussian PDF is

$$W(\boldsymbol{\xi}) = \left(1/\sqrt{2\pi}\right)^d e^{-\frac{1}{2}\xi^T\xi} \tag{3}$$

The uncertainty of some input parameter $k$ is expressed analytically as

$$k = \bar{k} + \xi_1\tilde{k} \tag{4}$$

where $\bar{k}$ is the mean value of $k$, $\tilde{k}$ the standard deviation, and $\xi_1$ an element of $\boldsymbol{\xi}$.

In the past, the basis chosen for the stochastic projection method was the set of polynomials orthogonal to the Gaussian distribution $W(\boldsymbol{\xi})$ of the input uncertainty and the method referred to as a polynomial chaos expansion (PCE). The series expansion given in Eq. (1) was formulated by Wiener[23] in 1938 and, in 1947 Cameron and Martin[24] proved that the series expansion is convergent for all square integrable functions. Because of the inability of the PCE method to resolve shocks and model the non-Gaussian flow parameters in turbulent flows, the method was mostly abandoned by the early 1970s (Refs. 20 and 25). In the 1990s, Ghanem and Spanos[17] revived the method for random vibrations solved with stochastic finite element methods. More recently, PCEs of the incompressible Navier–Stokes equations were formulated to quantify uncertainties in microchannel flow by Le Maître et al.[19] and low-Reynolds-number flow over a cylinder by Xiu et al.[21]

For a large class of nonlinear problems, the functional relationship between physical response and uncertainty parameters is linear or, at worst, weakly nonlinear. For such problems the PCE method is computationally efficient. In problems involving bifurcations, however, the response relationship is nonlinear, and polynomial expansions are computationally impractical. Thus, bifurcations of the type shown in Fig. 1 cannot be predicted by the PCE method. If a response is oscillatory, it is reasonable to expect the functional relationship of that response with the uncertainty parameter will also be oscillatory. This motivates the development of a new basis, the Fourier chaos. The spectral method using this basis is referred to as the Fourier chaos expansion (FCE). It will be shown that the FCE method predicts LCO response with low-order expansions, allowing the prediction of subcritical and supercritical responses.

## Fourier Chaos Expansion

The development of the FCE is analogous to the development of the PCE through a generalized framework as described by Xiu and his colleagues,[20] but the basis to be orthogonalized is not the monomial basis $1, x, x^2, \ldots$; instead, the development begins with the Fourier basis, that is, the set $\{1, \sin(n\xi_1), \cos(n\xi_1)\}$, where $n = 1, \ldots, \infty$. These trigonometric functions form a complete basis on any $2\pi$ interval in the $L_2$ space of square integrable functions,[26] and an examination of these functions when multiplied by the Gaussian PDF is shown in Figs. 2 and 3. The trigonometric functions are of limited amplitude over the real line, so that multiplication with the Gaussian PDF causes the product functions to reduce to zero very rapidly between $[-2\pi, 2\pi]$, which facilitates numerical integration. Because $2\pi \approx 6$ and $\boldsymbol{\xi}$ is of unit variance, an integration between $\pm 2\pi$ essentially captures a six-sigma approximation of the input distribution.

The construction of a general, multidimensional FCE begins with the one-dimensional Fourier chaos basis $\Psi_i(\xi_1)$ through order $p$ because higher dimension bases can be constructed from the former. To cause the basis to be orthogonal and normal with respect to the Gaussian PDF on the interval $[-2\pi, 2\pi]$, the well-known Gram–Schmidt process is employed.[27] The first function is a constant given by

$$\Psi_0(\xi_1) = \left[\int_{-2\pi}^{2\pi} W(x)\,\mathrm{d}x\right]^{-\frac{1}{2}} \tag{5}$$

$$= 1.0000000002 \tag{6}$$

$$\approx 1 \tag{7}$$

Noting that the weight function $W(\xi_1)$ is an even function and $\sin(\xi_1)$ is an odd function, the second basis function is simply $\sin(\xi_1)$. Normalization results in

$$\Psi_1(\xi_1) = 1.52087\sin(\xi_1) \tag{8}$$

The next function contains $\cos(\xi_1)$. Orthogonalization and normalization result in

$$\Psi_2(\xi_1) = 2.23725\cos(\xi_1) - 1.35696 \tag{9}$$

Proceeding in this manner and alternating between $\sin(n\xi_1)$ and $\cos(n\xi_1)$ results in the desired basis. The one-dimensional Fourier chaos, through order six, is shown in Table 1.

For two input uncertainties $\xi_1$ and $\xi_2$, the two-dimensional Fourier chaos is constructed from the one-dimensional Fourier chaos evaluated for $\xi_1$ and $\xi_2$, resulting in $\Psi_i(\xi_1)$ and $\Psi_i(\xi_2)$ with $i = 0, \ldots, p$. The two-dimensional FCE for $\alpha(t, \xi_1, \xi_2)$ is obtained from

$$\alpha(t, \xi_1, \xi_2) = \sum_{i=0}^{p} \sum_{j=0}^{i} \alpha_{k(i,j)}(t)\Psi_{i-j}(\xi_1)\Psi_j(\xi_2) \tag{10}$$

**Table 1 One-dimensional, orthonormal Fourier chaos**

| Order ($i = p$) | Fourier chaos $[\Psi_i(\xi_1)]$ |
|---|---|
| 0 | 1 |
| 1 | $1.52087\sin(\xi_1)$ |
| 2 | $2.23725\cos(\xi_1) - 1.35696$ |
| 3 | $1.8417\sin(2\xi_1) - 1.26822\sin(\xi_1)$ |
| 4 | $2.11036\cos(2\xi_1) - 2.395\cos(\xi_1) + 1.16703$ |
| 5 | $1.9396\sin(3\xi_1) - 1.68933\sin(2\xi_1) + 0.860469\sin(\xi_1)$ |
| 6 | $2.0387\cos(3\xi_1) - 2.11033\cos(2\xi_1) + 1.77151\cos(\xi_1) - 0.811519$ |

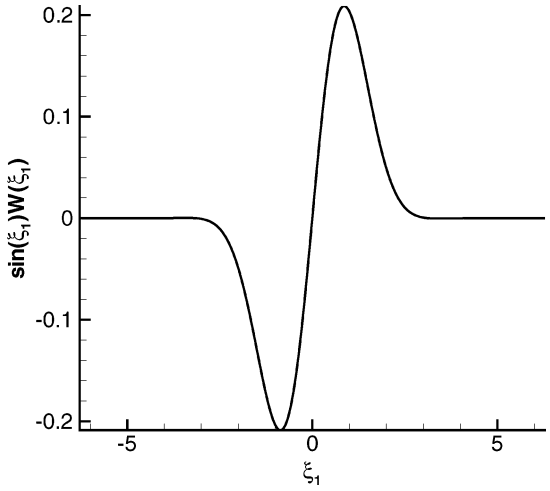


a) $\sin(\xi_1)W(\xi_1)$

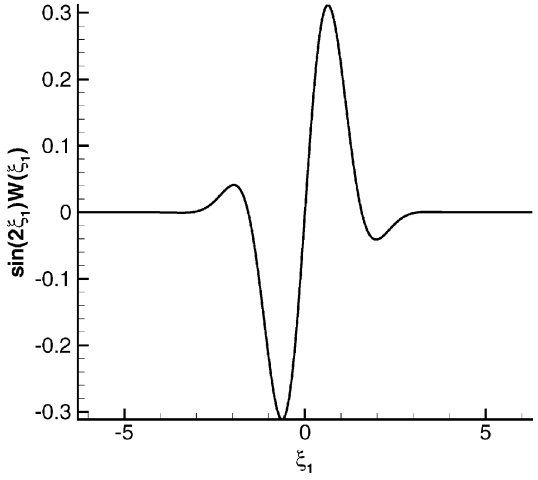


b) $\sin(2\xi_1)W(\xi_1)$

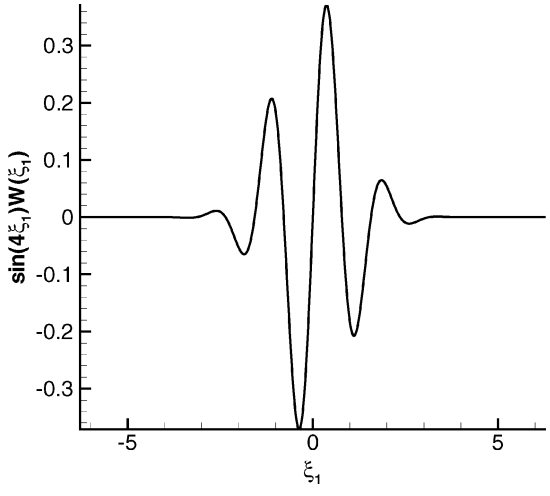


c) $\sin(4\xi_1)W(\xi_1)$

**Fig. 2 Examples of $\sin(n\xi_1)W(\xi_1)$.**

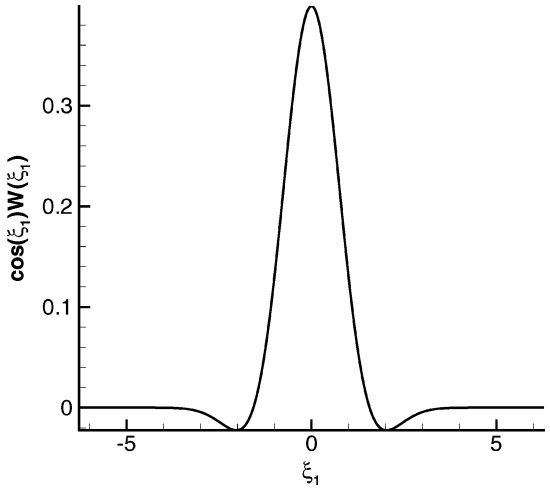


a) $\cos(\xi_1)W(\xi_1)$

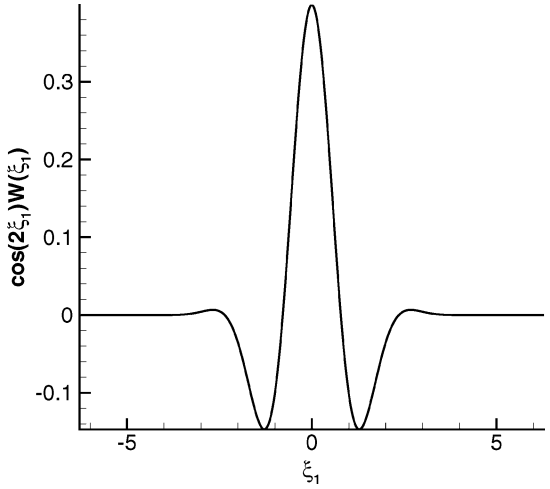


b) $\cos(2\xi_1)W(\xi_1)$

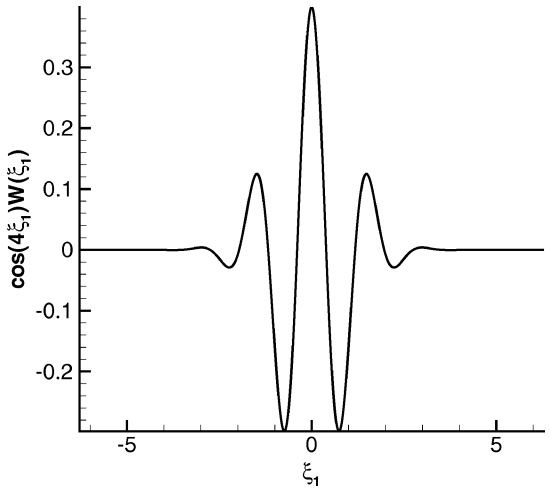


c) $\cos(4\xi_1)W(\xi_1)$

**Fig. 3 Examples of $\cos(n\xi_1)W(\xi_1)$.**

where $p$ is the order of the expansion and $k(i, j)$ is given by

$$k(i, j) = P(i, 2) - i + j \tag{11}$$

where Eq. (2) is used to obtain $P(i, 2)$.

## Pitch-and-Plunge Airfoil with a Cubic and Pentic Restoring Force

The FCE and the PCE methods were applied to the problem of determining the LCO response of a pitch-and-plunge airfoil. The standard notation[1,3] for a pitch-and-plunge airfoil is shown in Fig. 4.

Lee et al.[3] examined this configuration with a combined linear and cubic restoring force in both pitch and plunge. This type of configuration leads to a subcritical response without a turning-point bifurcation. Although it is possible that the turning-point bifurcation could be obtained with a modified cubic formulation, in this study the pitch equation is extended to include a pentic term in the restoring force to yield the desired subcritical behavior and provide

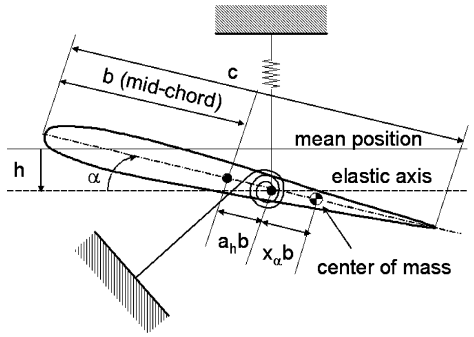


**Fig. 4 Pitch-and-plunge airfoil.**

insight into the highly nonlinear behavior with the PCE and FCE methods.[28,29] The equations of motion are then given by

$$\ddot{y} + x_\alpha \ddot{\alpha} + 2\zeta_y(\bar{\omega}/U^*)\dot{y} + (\bar{\omega}/U^*)^2\left(y + \beta_y y^3\right) = -(1/\pi\bar{m})C_L(\tau) \tag{12}$$

$$\left(x_\alpha \big/ r_\alpha^2\right)\ddot{y} + \ddot{\alpha} + 2(\zeta_\alpha/U^*)\dot{\alpha} + (1/U^{*2})\left(\alpha + \beta_\alpha\alpha^3 + \gamma_\alpha\alpha^5\right) = \left(2\big/\pi\bar{m}r_\alpha^2\right)C_M(\tau) \tag{13}$$

where $y = h/b$ is the nondimensional plunge displacement of the elastic axis; $\beta_y$, $\beta_\alpha$, and $\gamma_\alpha$ are the nonlinear spring constants; and $r_\alpha$ is the radius of gyration about the elastic axis. The mass ratio $\bar{m}$ is defined as

$$\bar{m} = m/\pi\rho b^2 \tag{14}$$

where $m$ is the mass of the airfoil and $\rho$ is the freestream density. The reduced velocity $U^*$ and the frequency ratio $\bar{\omega}$ are given by

$$U^* = U/b\omega_\alpha \tag{15}$$

$$\bar{\omega} = \omega_y/\omega_\alpha \tag{16}$$

where $U$ is the freestream velocity and $\omega_y$ and $\omega_\alpha$ are the uncoupled plunging and pitching mode undamped natural frequencies. Time differentiation is with respect to the nondimensional time $\tau$ given by

$$\tau = Ut/b \tag{17}$$

Following Lee et al.,[3] the plunge cubic spring constant $\beta_y$ the damping terms $\zeta_y$ and $\zeta_\alpha$ are set to zero, and

$$\bar{m} = 100 \qquad a_h = -0.5 \qquad x_\alpha = 0.25$$

$$\bar{\omega} = 0.2 \qquad r_\alpha = -0.5$$

The lift and pitching-moment coefficients $C_L(\tau)$ and $C_M(\tau)$ are as modeled by Jones.[30] Again, similar to Lee et al.'s work,[3] Eqs. (12) and (13) are rewritten as

$$c_0\ddot{y} + c_1\ddot{\alpha} + c_2\dot{y} + c_3\dot{\alpha} + c_4 y + c_5 y^3 + c_6\alpha + c_7 w_1 + c_8 w_2 + c_9 w_3 + c_{10} w_4 = f(\tau) \tag{18}$$

$$d_0\ddot{y} + d_1\ddot{\alpha} + d_2\dot{\alpha} + d_3\alpha + d_4\alpha^3 + d_5\alpha^5 + d_6\dot{y} + d_7 y + d_8 w_1 + d_9 w_2 + d_{10} w_3 + d_{11} w_4 = g(\tau) \tag{19}$$

The constants $c_0$ through $c_{10}$ and $d_0$ through $d_{11}$, the time-dependent variables $w_1(\tau)$ through $w_4(\tau)$, and the forcing terms $f(\tau)$ and $g(\tau)$ are shown in the Appendix. Because many of the details of this development have been omitted, the interested reader is referred to Lee et al.[3] Equations (18) and (19) are the starting point for the stochastic-projection method.

## Stochastic Projection

A complete analysis would include uncertainty in several parameters. For this study uncertainty was applied to only two input parameters, initial pitch angle and cubic pitch restoration coefficient. Lee et al.[3] showed that the Hopf bifurcation point and LCO amplitude are sensitive to the cubic spring coefficient in pitch $\beta_\alpha$ and the initial pitch angle $\alpha(0)$. Assuming a Gaussian distribution of these parameters, they are written as

$$\beta_\alpha = \bar{\beta}_\alpha + \xi_1\tilde{\beta}_\alpha \tag{20}$$

$$\alpha(0) = \bar{\alpha}(0) + \xi_2\tilde{\alpha}(0) \tag{21}$$

A hard spring is defined as $\beta_\alpha > 0$, and a soft spring as $\beta_\alpha < 0$. The hard spring leads to a supercritical response, whereas a soft spring gives a subcritical response with a turning point bifurcation. The uncertainty in $\beta_\alpha$ can be incorporated into Eq. (19) by rewriting the constant $d_4$ as

$$d_4 = \bar{d}_4 + \xi_1\tilde{d}_4 \tag{22}$$

where

$$\bar{d}_4 = \bar{\beta}_\alpha \big/ U^{*2} \tag{23}$$

$$\tilde{d}_4 = \tilde{\beta}_\alpha \big/ U^{*2} \tag{24}$$

The forcing functions in Eqs. (18) and (19) are rewritten by algebraic substitution of Eq. (21), resulting in

$$f(\tau) = \bar{f}(\tau) + \xi_2\tilde{f}(\tau) \tag{25}$$

where

$$\bar{f}(\tau) = (2/\bar{m})\left[\left(\tfrac{1}{2} - a_h\right)\bar{\alpha}(0) + y(0)\right]\left(\psi_1\varepsilon_1 e^{-\varepsilon_1\tau} + \psi_2\varepsilon_2 e^{-\varepsilon_2\tau}\right) \tag{26}$$

$$\tilde{f}(\tau) = (2/\bar{m})\left(\tfrac{1}{2} - a_h\right)\tilde{\alpha}(0)\left(\psi_1\varepsilon_1 e^{-\varepsilon_1\tau} + \psi_2\varepsilon_2 e^{-\varepsilon_2\tau}\right) \tag{27}$$

and

$$g(\tau) = \bar{g}(\tau) + \xi_2\tilde{g}(\tau) \tag{28}$$

where

$$\bar{g}(\tau) = -\frac{1 + 2a_h}{2r_\alpha^2}\bar{f}(\tau) \tag{29}$$

$$\tilde{g}(\tau) = -\frac{1 + 2a_h}{2r_\alpha^2}\tilde{f}(\tau) \tag{30}$$

The constants $\psi_1$, $\psi_2$, $\varepsilon_1$, and $\varepsilon_2$ are part of the Jones model for incompressible flow, and their values are given in the Appendix.

The responses $y$, $\alpha$, $w_1$, $w_2$, $w_3$, and $w_4$ are represented by expansions of the form shown in Eq. (1), where the upper limit $P(p, d)$ is given by Eq. (2) with $d = 2$. The stochastic projection is represented by replacing each of the preceding processes with their series expansions. Equation (19) is projected first and rewritten as

$$\sum_{i=0}^{P(p,d)} D_i\Psi_i + \bar{d}_4 \sum_{i=0}^{P(p,d)}\sum_{j=0}^{P(p,d)}\sum_{k=0}^{P(p,d)} \alpha_i\alpha_j\alpha_k\Psi_i\Psi_j\Psi_k + \tilde{d}_4 \sum_{i=0}^{P(p,d)}\sum_{j=0}^{P(p,d)}\sum_{k=0}^{P(p,d)} \alpha_i\alpha_j\alpha_k\xi_1\Psi_i\Psi_j\Psi_k + d_5 \sum_{i=0}^{P(p,d)}\sum_{j=0}^{P(p,d)}\sum_{k=0}^{P(p,d)}\sum_{l=0}^{P(p,d)}\sum_{m=0}^{P(p,d)} \alpha_i\alpha_j\alpha_k\alpha_l\alpha_m\Psi_i\Psi_j\Psi_k\Psi_l\Psi_m = \bar{g} + \xi_2\tilde{g} \tag{31}$$

where

$$D_i = d_0\ddot{y}_i + d_1\ddot{\alpha}_i + d_2\dot{\alpha}_i + d_3\alpha_i + d_6\dot{y}_i + d_7 y_i + d_8(w_1)_i + d_9(w_2)_i + d_{10}(w_3)_i + d_{11}(w_4)_i \tag{32}$$

A Galerkin approach[31] is implemented to solve for the time-dependent coordinates, where the inner product of an arbitrary function $\phi(\xi_1, \xi_2)$ with $\Psi_n(\xi_1, \xi_2)$ is given by

$$\langle \phi, \Psi_n \rangle = \frac{1}{2\pi} \int_{-I}^{I} \int_{-I}^{I} \phi \Psi_n W(\xi_1, \xi_2)\, \mathrm{d}\xi_1\, \mathrm{d}\xi_2 \tag{33}$$

where $n = 0, \ldots, P(p, d)$, and $I = \infty$ for the PCE, or $I = 2\pi$ for the FCE. Note the inner product also provides the expected value of the product of $\phi$ and $\Psi_n$. Multiplication of Eq. (31) with $\Psi_n$ and evaluation of the inner product results in

$$\sum_{i=0}^{P(p,d)} D_i \langle \Psi_i, \Psi_n \rangle + \bar{d}_4 \sum_{i=0}^{P(p,d)} \sum_{j=0}^{P(p,d)} \sum_{k=0}^{P(p,d)} \alpha_i \alpha_j \alpha_k \langle \Psi_i \Psi_j \Psi_k, \Psi_n \rangle + \tilde{d}_4 \sum_{i=0}^{P(p,d)} \sum_{j=0}^{P(p,d)} \sum_{k=0}^{P(p,d)} \alpha_i \alpha_j \alpha_k \langle \xi_1 \Psi_i \Psi_j \Psi_k, \Psi_n \rangle + d_5 \sum_{i=0}^{P(p,d)} \sum_{j=0}^{P(p,d)} \sum_{k=0}^{P(p,d)} \sum_{l=0}^{P(p,d)} \sum_{m=0}^{P(p,d)} \alpha_i \alpha_j \alpha_k \alpha_l \alpha_m \times \langle \Psi_i \Psi_j \Psi_k \Psi_l \Psi_m, \Psi_n \rangle = \bar{g} \langle 1, \Psi_n \rangle + \tilde{g} \langle \xi_2, \Psi_n \rangle \tag{34}$$

For any orthogonal basis, the only terms surviving in the first summation are those multiplied by the variance $\langle \Psi_n, \Psi_n \rangle$. Division by the variance gives the desired expression:

$$D_n + \bar{d}_4 \sum_{i=0}^{P(p,d)} \sum_{j=0}^{P(p,d)} \sum_{k=0}^{P(p,d)} \alpha_i \alpha_j \alpha_k c_{ijkn} + \tilde{d}_4 \sum_{i=0}^{P(p,d)} \sum_{j=0}^{P(p,d)} \sum_{k=0}^{P(p,d)} \times \alpha_i \alpha_j \alpha_k c_{1ijkn} + d_5 \sum_{i=0}^{P(p,d)} \sum_{j=0}^{P(p,d)} \sum_{k=0}^{P(p,d)} \sum_{l=0}^{P(p,d)} \sum_{m=0}^{P(p,d)} \times \alpha_i \alpha_j \alpha_k \alpha_l \alpha_m c_{ijklmn} = \bar{g} \frac{\langle 1, \Psi_n \rangle}{\langle \Psi_n, \Psi_n \rangle} + \tilde{g} \frac{\langle \xi_2, \Psi_n \rangle}{\langle \Psi_n, \Psi_n \rangle} \tag{35}$$

where

$$c_{ijkn} \equiv \frac{\langle \Psi_i \Psi_j \Psi_k, \Psi_n \rangle}{\langle \Psi_n, \Psi_n \rangle} \tag{36}$$

$$c_{1ijkn} \equiv \frac{\langle \xi_1 \Psi_i \Psi_j \Psi_k, \Psi_n \rangle}{\langle \Psi_n, \Psi_n \rangle} \tag{37}$$

$$c_{ijklmn} \equiv \frac{\langle \Psi_i \Psi_j \Psi_k \Psi_l \Psi_m, \Psi_n \rangle}{\langle \Psi_n, \Psi_n \rangle} \tag{38}$$

Note that the multipliers $c_{ijkn}$, $c_{1ijkn}$, and $c_{ijklmn}$ need to be computed only once. A similar procedure performed on Eq. (18) results in

$$c_0\ddot{y}_n + c_1\ddot{\alpha}_n + c_2\dot{y}_n + c_3\dot{\alpha}_n + c_4 y_n + c_5\alpha_n + c_7(w_1)_n + c_8(w_2)_n + c_9(w_3)_n + c_{10}(w_4)_n + c_5 \sum_{i=0}^{P(p,d)} \sum_{j=0}^{P(p,d)} \sum_{k=0}^{P(p,d)} y_i y_j y_k c_{ijkn} = \bar{f} \frac{\langle 1, \Psi_n \rangle}{\langle \Psi_n, \Psi_n \rangle} + \tilde{f} \frac{\langle \xi_2, \Psi_n \rangle}{\langle \Psi_n, \Psi_n \rangle} \tag{39}$$

The initial condition on $\alpha$ is also stochastically projected. It can be shown that the initial pitch angle becomes

$$\alpha_n(0) = \bar{\alpha}(0) \frac{\langle 1, \Psi_n \rangle}{\langle \Psi_n, \Psi_n \rangle} + \tilde{\alpha}(0) \frac{\langle \xi_2, \Psi_n \rangle}{\langle \Psi_n, \Psi_n \rangle} \tag{40}$$

## Numerical Procedure

By letting $\boldsymbol{x}_1 = \boldsymbol{\alpha}$, $\boldsymbol{x}_2 = \dot{\boldsymbol{\alpha}}$, $\boldsymbol{x}_3 = \boldsymbol{y}$, $\boldsymbol{x}_4 = \dot{\boldsymbol{y}}$, $\boldsymbol{x}_5 = \boldsymbol{w}_1$, $\boldsymbol{x}_6 = \boldsymbol{w}_2$, $\boldsymbol{x}_7 = \boldsymbol{w}_3$, and $\boldsymbol{x}_8 = \boldsymbol{w}_4$, Eqs. (35) and (39) are reduced to the following first-order, vector, ordinary differential equations:

$$\dot{\boldsymbol{x}}_1 = \boldsymbol{x}_2 \tag{41}$$

$$\dot{\boldsymbol{x}}_2 = (c_0\boldsymbol{A} - d_0\boldsymbol{B})/(d_0c_1 - c_0d_1) \tag{42}$$

$$\dot{\boldsymbol{x}}_3 = \boldsymbol{x}_4 \tag{43}$$

$$\dot{\boldsymbol{x}}_4 = (-c_1\boldsymbol{A} + d_1\boldsymbol{B})/(d_0c_1 - c_0d_1) \tag{44}$$

$$\dot{\boldsymbol{x}}_5 = \boldsymbol{x}_1 - \varepsilon_1\boldsymbol{x}_5 \tag{45}$$

$$\dot{\boldsymbol{x}}_6 = \boldsymbol{x}_1 - \varepsilon_2\boldsymbol{x}_6 \tag{46}$$

$$\dot{\boldsymbol{x}}_7 = \boldsymbol{x}_3 - \varepsilon_1\boldsymbol{x}_7 \tag{47}$$

$$\dot{\boldsymbol{x}}_8 = \boldsymbol{x}_3 - \varepsilon_2\boldsymbol{x}_8 \tag{48}$$

where

$$\boldsymbol{A} = d_2\boldsymbol{x}_2 + d_3\boldsymbol{x}_1 + \bar{d}_4\boldsymbol{\alpha}_{\text{mean}} + \tilde{d}_4\boldsymbol{\alpha}_{\text{sd}} + d_{11}\boldsymbol{\alpha}_{\text{pentic}} + d_5\boldsymbol{x}_4 + d_6\boldsymbol{x}_3 + d_7\boldsymbol{x}_5 + d_8\boldsymbol{x}_6 + d_9\boldsymbol{x}_7 + d_{10}\boldsymbol{x}_8 - \boldsymbol{g}(\tau) \tag{49}$$

$$\boldsymbol{B} = c_2\boldsymbol{x}_4 + c_3\boldsymbol{x}_2 + c_4\boldsymbol{x}_3 + c_5\boldsymbol{y}_{\text{mean}} + c_6\boldsymbol{x}_1 + c_7\boldsymbol{x}_5 + c_8\boldsymbol{x}_6 + c_9\boldsymbol{x}_7 + c_{10}\boldsymbol{x}_8 - \boldsymbol{f}(\tau) \tag{50}$$

The elements of the nonlinear terms are given by such terms as

$$(\alpha_{\text{mean}})_n = \sum_{i=0}^{P(p,d)} \sum_{j=0}^{P(p,d)} \sum_{k=0}^{P(p,d)} \alpha_i \alpha_j \alpha_k c_{ijkn} \tag{51}$$

To this point, the method is general and the basis not yet specified. If a PCE is employed, the appropriate basis would be the Hermite polynomials because they are the unique set of polynomials orthogonal to the Gaussian PDF.[17] The evaluation of the inner products for the Hermite polynomials are straightforward.[32] If an FCE is employed, a numerical integration of the inner products is accomplished. In both cases, the number of nonzero multipliers grows rapidly with the order of expansion.

Any standard integration technique can be implemented on Eqs. (41–48). The forward Euler method was used in this study. The time step $\Delta\tau$ should be 1/256 of the shorter period of the two modes (pitch or plunge) to maintain accuracy of the amplitude and period of the oscillation.[3] This requirement is satisfied with $\Delta\tau = 0.1$. The mean and standard deviation for a hard spring ($\beta_\alpha > 0$) were chosen as

$$\bar{\beta}_\alpha = 3.0 \tag{52}$$

$$\tilde{\beta}_\alpha = 0.3 \tag{53}$$

and for a soft spring ($\beta_\alpha < 0$) they were

$$\bar{\beta}_\alpha = -3.0 \tag{54}$$

$$\tilde{\beta}_\alpha = 0.3 \tag{55}$$

The mean and standard deviation of the initial pitch are

$$\bar{\alpha} = 0.0 \tag{56}$$

$$\tilde{\alpha} = 0.2 \tag{57}$$

For comparisons of the FCE and PCE methods, 10,000 Monte Carlo simulations were run on the deterministic governing equations [Eqs. (18) and (19)] to estimate the PDFs of the subcritical and supercritical responses. Ten-thousand simulations were deemed adequate based on the convergence of the mean value to three significant digits. For each realization of $\beta_\alpha$ and $\alpha(0)$, a time history such as the

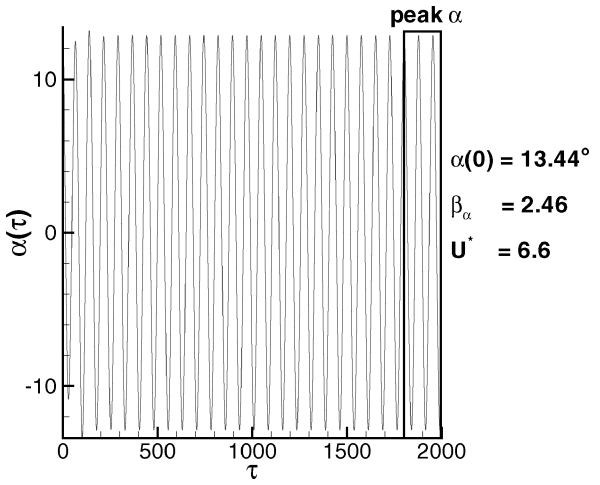


a) Typical time history

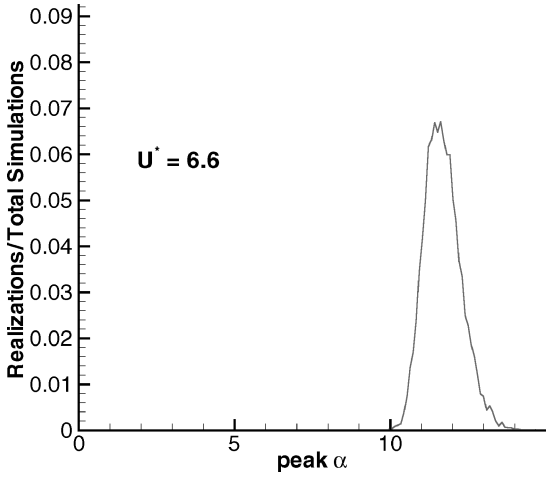


b) PDF of peak $\alpha$

**Fig. 5 Time history and PDF at $U^* = 6.6$.**

one shown in Fig. 5a is computed. The peak $\alpha$ during the last 10% of the solution is saved as a realization of the response. Integrating far out in time and examining only the last 10% ensures the solution is free of starting transients. For 10,000 MCSs on the deterministic governing equations, the PDF in Fig. 5b results. From the peak PDF value of $\alpha$ for each velocity, bifurcation diagrams such as the one shown in Fig. 1 are generated.

To capture the peak $\alpha$ in the last 10% of the time interval with either stochastic projection method, the coefficients $\alpha_i(\tau)$ are saved at every time step in this interval. An MCS is then performed on the expansion

$$\alpha(\tau, \xi_1, \xi_2) = \sum_{i=0}^{P(p,d)} \alpha_i(\tau)\Psi_i(\xi_1, \xi_2) \qquad 0.9\tau_{\max} \le \tau \le \tau_{\max} \quad (58)$$

which is significantly less expensive than running Monte Carlo simulations on the governing equations. A check is made for the peak $\alpha$ at each computation. The peak value over each time interval is saved as a realization.

## Results

As evident from Eq. (35), the pentic summation generates a large number of terms that can result in large computer run times. Thus, in order to initially observe convergence properties of PCEs and FCEs with progressively higher-order expansions, $\gamma_\alpha$ [see Eq. (13)] was set to zero. The results for $U^* = 6.5$ and a hard spring are shown in Fig. 6.

Figure 6a shows that although a fourth-order PCE identifies only a possible range of pitch angles the fourth-order FCE is already

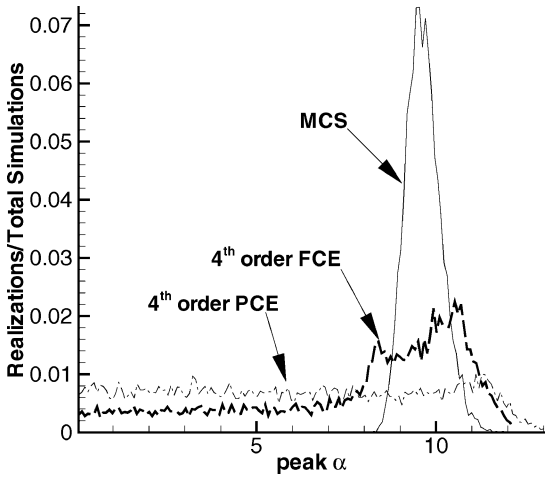


a) MCS vs fourth-order PCE and FCE

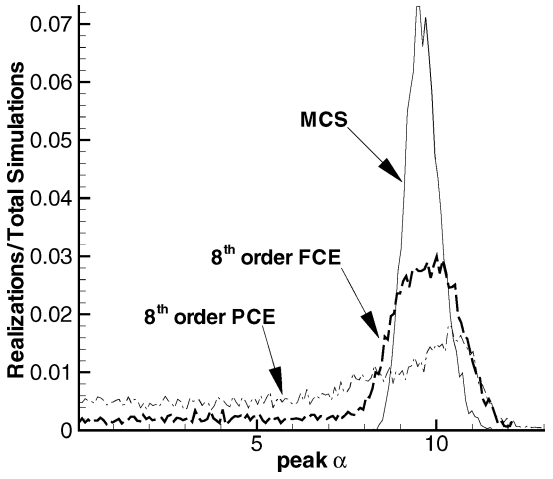


b) MCS vs eighth-order PCE and FCE

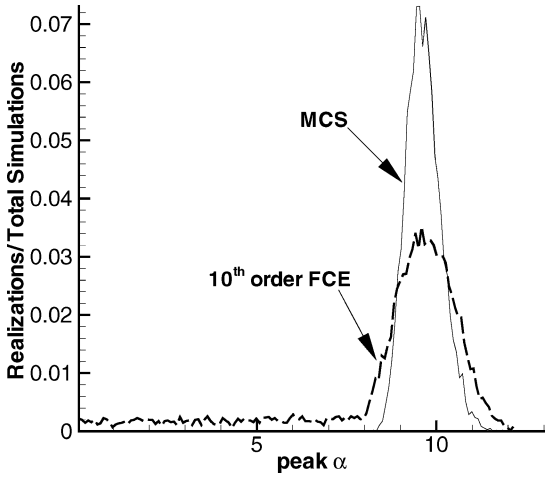


c) MCS vs tenth-order FCE

**Fig. 6 PDFs of the supercritical response at $U^* = 6.5$.**

beginning to show evidence of LCO. The difference between the two methods is even more dramatic in Fig. 6b, where the eighth-order PCE still has not captured the range of LCO. Figure 6c shows that the tenth-order FCE is continuing to converge to the PDF given by the MCS.

The excessive tail of both the PCE and FCE is an artifact of convergence, and its explanation is closely related to the reason for failure of the PCE to predict the proper PDF. A physical interpretation of the stochastic projection method indicates that at any particular time $t = T$ the series solution attempts to fit a curve to the function

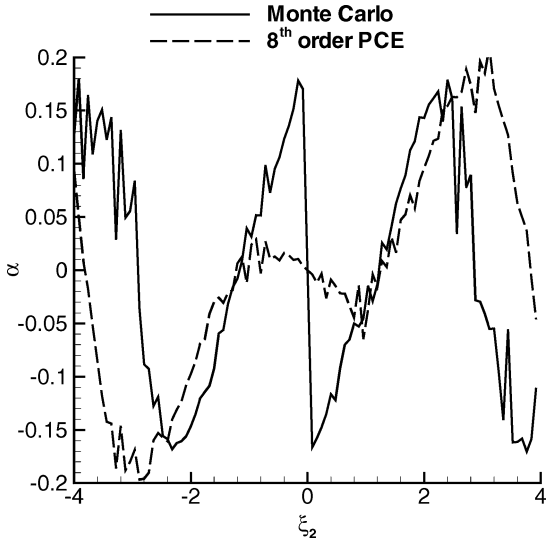


a) MCS vs eighth-order PCE

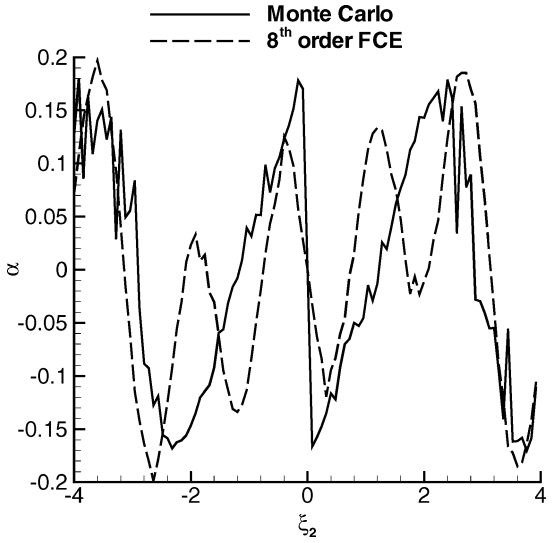


b) MCS vs eighth-order FCE

**Fig. 7 $\alpha(t, \xi)$ at $t = 2000$ vs $\xi_2$.**

defined by the variation of $\alpha(t, \xi)$ with $\xi$, that is, the output response as a function of the input random variable. In Fig. 7, the Monte Carlo response for $\alpha(T, \xi_1, \xi_2)$, where $T = 2000$, is strongly dependent on the sign of the initial pitch and results in a discontinuity at $\xi_2 = 0$. A large number of PCE polynomials would be required to fit such a curve. In Fig. 7a, the amplitude of the pitch angle for the eighth-order PCE is much smaller than the MCS predictions in the range of $-1.5 < \xi_2 < 1.5$. An MCS on this projection leads to the excessive tail for the PCE in Fig. 6b. That is, realizations near zero are obtained from the PCE that are not obtained from the MCS. In contrast, the same (eighth)-order FCE locates and closely approximates this discontinuity (Fig. 7b). Because the slope of this approximation is finite, an MCS on this projection will again lead to numerous realizations near zero amplitude, resulting in the excessive tail. The overall appearance of the FCE response curve, however, is close enough to the Monte Carlo results to obtain reasonable predictions. Thus, for this model problem the Fourier chaos is a more optimal basis than the polynomial chaos for predicting LCO. The high-frequency wiggles in Figs. 7a and 7b are a result of the variations in the cubic spring constant. If $\xi_1$ were held fixed, these projections would be smooth.

Finally, although the FCE remained stable at a $\Delta\tau = 0.1$ for all order expansions, the eighth-order PCE was unstable at this time step. This instability was caused by the large variation in the multipliers of the nonlinear terms, which ranged from order one $\mathcal{O}(1)$ to $\mathcal{O}(10^{10})$. In contrast, the multipliers for the FCE method ranged from $\mathcal{O}(1)$ to $\mathcal{O}(100)$. To achieve stability for the eighth-order PCE, the time step was halved. CPU times are shown in Table 2. Both the PCE and FCE rapidly lose efficiency as the order of the expansion increases. This is to be expected because the number of nonlinear terms to be computed grows geometrically with the increasing order of expansion. However, with the choice of an FCE, reasonable predictions for the PDF of the responses are obtained at low-order expansions, where the FCE is efficient.

**Table 2 CPU time, s**

| Method | $p = 0$ | $p = 4$ | $p = 8$ | $p = 10$ |
|---|---|---|---|---|
| MCS | 195.7 | —— | —— | —— |
| PCE | —— | 8.297 | 275.7 | —— |
| FCE | —— | 7.030 | 167.8 | 774.5 |

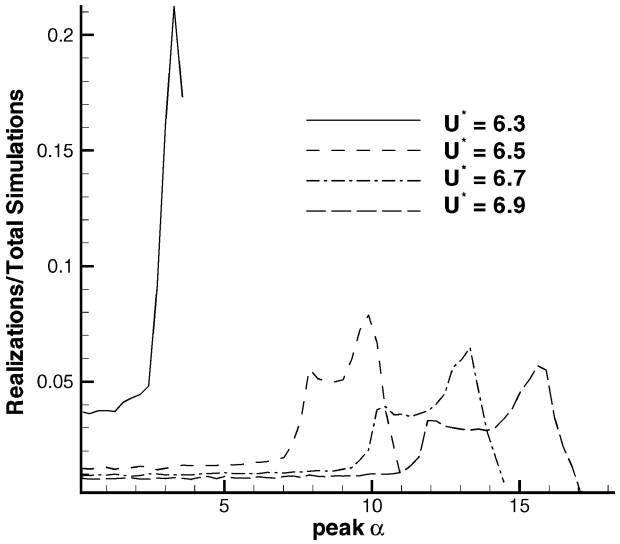


a) PDFs of peak $\alpha$ for $\beta_\alpha > 0$

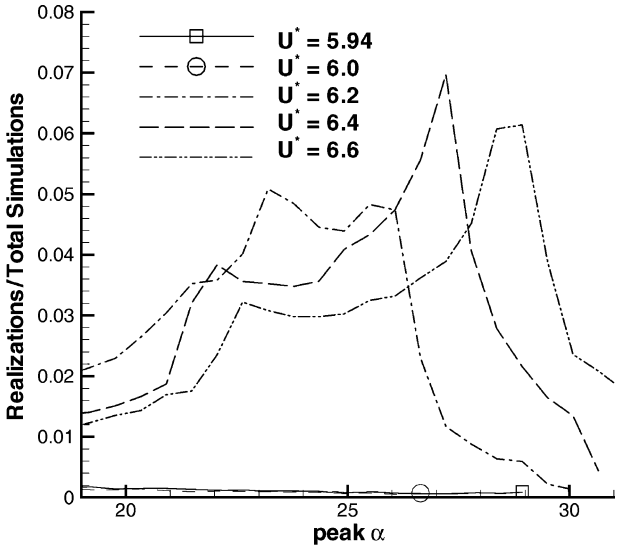


b) PDFs of peak $\alpha$ for $\beta_\alpha < 0$

**Fig. 8 PDFs with a fourth-order FCE**

Because the Fourier chaos, more so than the polynomial chaos, was an optimal basis, both in terms of convergence properties and computational efficiency, only the FCE method is shown for the remainder of this study. With the pentic term $\gamma_\alpha$ [see Eq. (13)] included, trial and error indicated that a value of $\gamma_\alpha = 20$ would provide the types of responses shown in Fig. 1. PDFs for various values of $U^*$ were generated with both MCS and a fourth-order FCE. Figures 8a and 8b show PDFs generated for the hard spring ($\beta_\alpha > 0$) and soft spring ($\beta_\alpha < 0$), respectively.

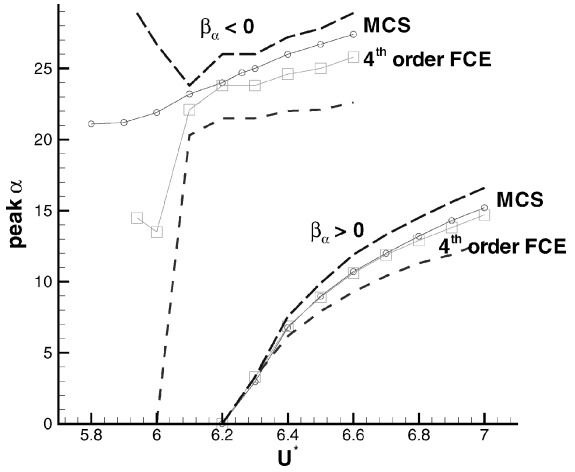


**Fig. 9 Bifurcation diagram with a fourth-order FCE.**

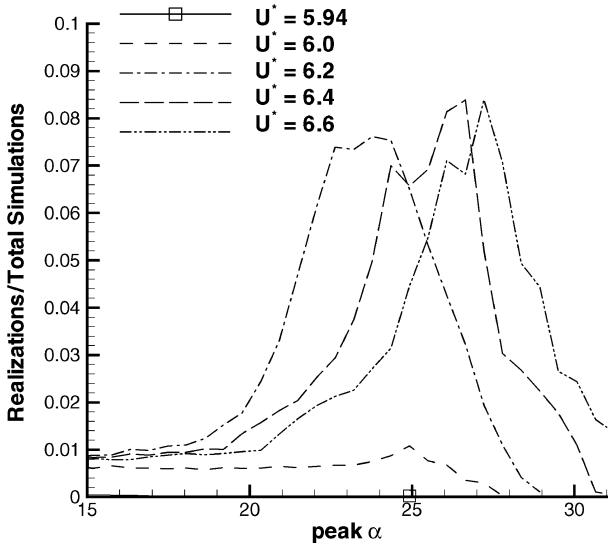


**Fig. 10 PDFs of peak $\alpha$ for $\beta_\alpha < 0$ with a sixth-order FCE.**

The rapid rises on the supercritical responses in Fig. 8a are well defined and allow an estimation of the peak value of the PDFs from the algebraic mean of the two clearly defined local maxima. The subcritical case, however, was not easy to interpret. The turning-point bifurcation was determined through a trial-and-error variation in $U^*$. In Fig. 8b, the FCE predicted oscillations at $U^* \approx 5.94$ but could not predict the range of LCO until $U^* \approx 6.2$. Figure 9 is the bifurcation diagram based on the PDFs in Figs. 8a and 8b. The location of the Hopf bifurcation point ($U^* \approx 6.20$) and the supercritical response with FCE are in excellent agreement with the MCS. The FCE prediction of the turning-point bifurcation ($U^* \approx 5.94$) is within 3% of the MCS prediction ($U^* \approx 5.80$). The dashed lines in Fig. 9 are estimation bounds, which are defined by the locations of the local maxima for each PDF. For the subcritical case, the estimation bounds improve dramatically just past the turning point bifurcation.

To determine the effects of higher-order expansions for the subcritical case, PDFs were recomputed with a sixth-order FCE. As seen in Fig. 10, peaks are easily discernible. The bifurcation diagram corresponding to Fig. 10 is shown in Fig. 11. Although the range of LCO at the turning-point bifurcation is still difficult to determine, the LCO value is in much better agreement with the MCS predictions at all other velocities.

The MCS required approximately 200 s of CPU time to compute 10,000 realizations. The fourth-order FCE required approximately 40 s of run time for the same number of realizations. Note that this is an order of magnitude greater than the fourth-order FCE with $\gamma_\alpha = 0$ (see Table 2). This order-of-magnitude increase in run time is directly attributable to the inclusion of the fifth-order terms. The

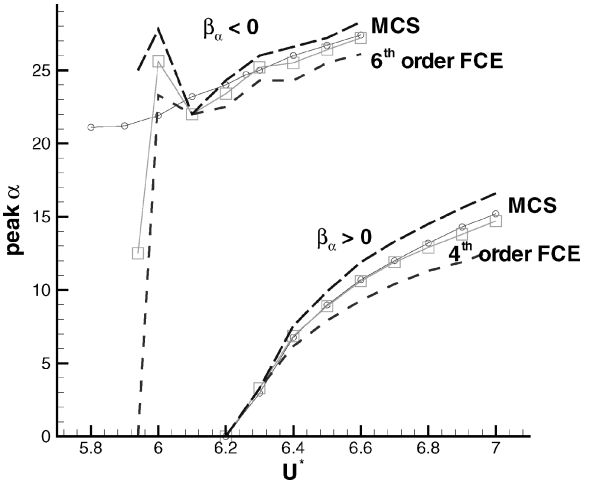


**Fig. 11 Bifurcation diagram with a fourth- and sixth-order FCE.**

sixth-order FCE required approximately 1300 s. Although computational efficiency decreases as the order of expansion increases, the FCE predicts bifurcation at a low enough order to remain useful. As a final note, a sixth-order PCE required approximately 12,000 s of CPU time. This dramatic increase in run time was attributed not only to the inclusion of the fifth-order terms, but more directly to the time-step restriction already mentioned that required an order-of-magnitude reduction in $\Delta\tau$ in order for the integration scheme to remain stable. Additionally, the sixth-order PCE provided relatively little information as a result of its slower convergence.

## Conclusions

A new basis, the Fourier chaos, has been developed for the stochastic projection method in problems exhibiting LCO. The PCE method could not predict LCO response for the pitch-and-plunge airfoil, whereas the FCE method could predict both subcritical and supercritical responses. The FCE predictions were made with low-order expansions and high-order nonlinearities. The bifurcation diagrams generated with this approximate method compare well to Monte Carlo simulations.

## Appendix: Constants and Variables for the Equations of Motion

The constants in the equation of motion for plunge, Eq. (18), are defined as[3]

$$c_0 = 1 + 1/\mu \tag{A1}$$

$$c_1 = x_\alpha - a_h/\mu \tag{A2}$$

$$c_2 = 2\zeta_y(\bar{\omega}/U^*) + (2/\mu)(1 - \psi_1 - \psi_2) \tag{A3}$$

$$c_3 = \left[1 + 2\left(\tfrac{1}{2} - a_h\right)(1 - \psi_1 - \psi_2)\right]\Big/\mu \tag{A4}$$

$$c_4 = (\bar{\omega}/U^*)^2 + (2/\mu)(\psi_1\varepsilon_1 + \psi_2\varepsilon_2) \tag{A5}$$

$$c_5 = \beta_y(\bar{\omega}/U^*)^2 \tag{A6}$$

$$c_6 = (2/\mu)\left[(1 - \psi_1 - \psi_2) + \left(\tfrac{1}{2} - a_h\right)(\psi_1\varepsilon_1 + \psi_2\varepsilon_2)\right] \tag{A7}$$

$$c_7 = (2/\mu)\psi_1\varepsilon_1\left[1 - \left(\tfrac{1}{2} - a_h\right)\varepsilon_1\right] \tag{A8}$$

$$c_8 = (2/\mu)\psi_2\varepsilon_2\left[1 - \left(\tfrac{1}{2} - a_h\right)\varepsilon_2\right] \tag{A9}$$

$$c_9 = -(2/\mu)\psi_1\varepsilon_1^2 \tag{A10}$$

$$c_{10} = -(2/\mu)\psi_2\varepsilon_2^2 \tag{A11}$$

The constants in the equation of motion for pitch, Eq. (19), are defined as[3]

$$d_0 = \frac{x_\alpha}{r_\alpha^2} - \frac{a_h}{\mu r_\alpha^2} \tag{A12}$$

$$d_1 = 1 + \frac{1 + 8a_h^2}{8\mu r_\alpha^2} \tag{A13}$$

$$d_2 = 2\frac{\zeta_\alpha}{U^*} + \frac{1 - 2a_h}{2\mu r_\alpha^2} - \frac{(1 + 2a_h)(1 - 2a_h)(1 - \psi_1 - \psi_2)}{2\mu r_\alpha^2} \tag{A14}$$

$$d_3 = \frac{1}{U^{*2}} - \frac{(1 + 2a_h)(1 - \psi_1 - \psi_2)}{\mu r_\alpha^2} - \frac{(1 + 2a_h)(1 - 2a_h)(\psi_1\varepsilon_1 + \psi_2\varepsilon_2)}{2\mu r_\alpha^2} \tag{A15}$$

$$d_4 = \frac{\beta_\alpha}{U^{*2}} \tag{A16}$$

$$d_5 = \frac{\gamma_\alpha}{U^{*2}} \tag{A17}$$

$$d_6 = -\frac{(1 + 2a_h)(1 - \psi_1 - \psi_2)}{\mu r_\alpha^2} \tag{A18}$$

$$d_7 = -\frac{(1 + 2a_h)(\psi_1\varepsilon_1 + \psi_2\varepsilon_2)}{\mu r_\alpha^2} \tag{A19}$$

$$d_8 = -\frac{(1 + 2a_h)\psi_1\varepsilon_1\left[1 - \left(\frac{1}{2} - a_h\right)\varepsilon_1\right]}{\mu r_\alpha^2} \tag{A20}$$

$$d_9 = -\frac{(1 + 2a_h)\psi_2\varepsilon_2\left[1 - \left(\frac{1}{2} - a_h\right)\varepsilon_2\right]}{\mu r_\alpha^2} \tag{A21}$$

$$d_{10} = \frac{(1 + 2a_h)\psi_1\varepsilon_1^2}{\mu r_\alpha^2} \tag{A22}$$

$$d_{11} = \frac{(1 + 2a_h)\psi_2\varepsilon_2^2}{\mu r_\alpha^2} \tag{A23}$$

The time-dependent variables $w_1(\tau)$ through $w_4(\tau)$ and the forcing terms $f(\tau)$ and $g(\tau)$ in Eqs. (18) and (19) are given by

$$w_1(\tau) = \int_0^\tau e^{-\varepsilon_1(\tau - \sigma)}\alpha(\sigma)\,\mathrm{d}\sigma \tag{A24}$$

$$w_2(\tau) = \int_0^\tau e^{-\varepsilon_2(\tau - \sigma)}\alpha(\sigma)\,\mathrm{d}\sigma \tag{A25}$$

$$w_3(\tau) = \int_0^\tau e^{-\varepsilon_1(\tau - \sigma)}y(\sigma)\,\mathrm{d}\sigma \tag{A26}$$

$$w_4(\tau) = \int_0^\tau e^{-\varepsilon_2(\tau - \sigma)}y(\sigma)\,\mathrm{d}\sigma \tag{A27}$$

$$f(\tau) = \frac{2}{\bar{m}}\left[\left(\frac{1}{2} - a_h\right)\alpha(0) + y(0)\right]\left(\psi_1\varepsilon_1 e^{-\varepsilon_1\tau} + \psi_2\varepsilon_2 e^{-\varepsilon_2\tau}\right) \tag{A28}$$

$$g(\tau) = -\frac{1 + 2a_h}{2r_\alpha^2}f(\tau) \tag{A29}$$

where $\psi_1 = 0.165$, $\psi_2 = 0.335$, $\varepsilon_1 = 0.0455$, and $\varepsilon_2 = 0.3$ (Ref. 30).

## Acknowledgment

This project was sponsored and funded by the U.S. Air Force Research Laboratory, AFRL/VASD, Wright–Patterson Air Force Base, Ohio.

## References

[1]Fung, Y., *An Introduction to the Theory of Aeroelasticity*, Dover Pub., New York, 1969, pp. 160–165.

[2]Bunton, R. W., and Denegri, C. M., "Limit Cycle Oscillation Characteristics of Fighter Aircraft," *Journal of Aircraft*, Vol. 37, No. 5, 2000, pp. 916–918.

[3]Lee, B., Jiang, L., and Wong, Y., "Flutter of an Airfoil with a Cubic Nonlinear Restoring Force," AIAA Paper 98-1725, April 1998.

[4]Matsushita, H., Saitoh, K., and Gránásy, P., "Wind Tunnel Investigation of Transonic Limit Cycle Oscillation," AIAA Paper 98-1725, April 1998.

[5]Tang, L., Bartels, R., Chen, P., and Liu, D., "Simulation of Transonic Limit Cycle Oscillation using a CFD Time Marching Method," AIAA Paper 2001-1292, April 2001.

[6]Beran, P., "Computation of Limit Cycle Oscillation Using a Direct Method," AIAA Paper 99-1462, April 1999.

[7]Seydel, R., *Practical Bifurcation and Stability Analysis: From Equilibrium to Chaos*, Elsevier Science, New York, 1988, Chap. 2.

[8]Lindsley, N., Beran, P., and Pettit, C., "Effects of Uncertainty on Nonlinear Plate Aeroelastic Response," AIAA Paper 2002-1271, 2002.

[9]Melchers, R., *Structural Reliability Analysis and Prediction*, 2nd ed., Wiley, New York, 1999, Chap. 10.

[10]Wojtkiewicz, S., Eldred, M., Field, R., Urbina, A., and Red-Horse, J., "Uncertainty Quantification in Large Computational Engineering Models," AIAA Paper 2001-1455, April 2001.

[11]Kiureghian, A. D., "The Geometry of Random Vibrations and Solutions by FORM and SORM," *Probabilistic Engineering Mechanics*, Vol. 15, No. 1, 2000, pp. 81–90.

[12]Ghanem, R., "A Comparative Analysis of FORM/SORM and Polynomial Chaos Expansions for Highly Nonlinear Systems," *Engineering Mechanics: Proceedings of the 11th Conference*, Vol. 1, edited by Y. Lin and D. Ghiocel, Engineering Mechanics Div., American Society of Civil Engineers, New York, 1996, pp. 535–538.

[13]Beran, P., and Silva, W., "Reduced Order Modeling: New Approaches to Computational Physics," AIAA Paper 2001-0853, Jan. 2001.

[14]Beran, P. S., and Pettit, C. L., "Prediction of Nonlinear Panel Response Using Proper Orthogonal Decomposition," AIAA Paper 2001-1292, April 2001.

[15]Pettit, C. L., and Beran, P. S., "Reduced-Order Modeling for Flutter Prediction," AIAA Paper 2000-1446, April 2000.

[16]Pettit, C. L., and Beran, P. S., "Application of Proper Orthogonal Decomposition to the Discrete Euler Equations," *International Journal for Numerical Methods in Engineering*, Vol. 55, No. 4, Oct. 2002, pp. 479–497.

[17]Ghanem, R. G., and Spanos, P. D., *Stochastic Finite Element Methods: A Spectral Approach*, Springer-Verlag, New York, 1991, Chap. 2.

[18]Li, R., and Ghanem, R., "Adaptive Polynomial Chaos Expansions Applied to Statistics of Extremes in Non-Linear Random Vibration," *Probabilistic Engineering Mechanics*, Vol. 13, No. 2, 1997, pp. 125–136.

[19]Le Maître, O. P., Knio, O. M., Najm, H. N., and Ghanem, R. G., "A Stochastic Projection Method for Fluid Flow," *Journal of Computational Physics*, Vol. 173, No. 2, 2001, pp. 481–511.

[20]Xiu, D., and Karniadakis, G. E., "Modeling Flow Uncertainty in Flow Simulations via Generalized Polynomial Chaos," *Journal of Computational Physics*, Vol. 187, No. 1, May 2003, pp. 137–168.

[21]Xiu, D., Lucor, D., Su, C.-H., and Karniadakis, G. E., "Stochastic Modeling of Flow-Structure Interactions Using Generalized Polynomial Chaos," *Journal of Fluids Engineering*, Vol. 124, No. 1, March 2002, pp. 51–58.

[22]Xiu, D., and Karniadakis, G. E., "Modeling Uncertainty in Steady State Diffusion Problems via Generalized Polynomial Chaos," *Computational Methods in Applied Mechanics*, Vol. 191, No. 43, 2002, pp. 4927–4948.

[23]Wiener, N., "The Homogeneous Chaos," *American Journal of Mathematics*, Vol. 60, 1938, pp. 897–936.

[24]Cameron, R., and Martin, W., "The Orthogonal Development of Nonlinear Functionals in Series of Fourier-Hermite Functionals," *Annals of Mathematics*, Vol. 48, No. 2, 1947, pp. 385–392.

[25]Chorin, A. J., "Guassian Fields and Random Flows," *Journal of Fluid Mechanics*, Vol. 63, No. 1, 1974, pp. 21–32.

[26]Arfken, G. B., and Weber, H. J., *Mathematical Methods for Physicists*, 4th ed., Academic Press, San Diego, 1995, pp. 760–793.

[27]Atkinson, K. E., *An Introduction to Numerical Analysis*, 2nd ed., Wiley, New York, 1989, pp. 197–246.

[28]Millman, D. R., King, P. I., and Beran, P. S., "A Stochastic Approach for Predicting Bifurcation of a Pitch and Plunge Airfoil," AIAA Paper 2003-3515, June 2003.

[29]Pettit, C. L., and Beran, P. S., "Effects of Parametric Uncertainty on Airfoil Limit Cycle Oscillation," *Journal of Aircraft*, Vol. 40, No. 5, 2003, pp. 1004–1006.

[30]Jones, R., "The Unsteady Lift of a Wing of Finite Aspect Ratio," NACA Rept. 681, 1940.

[31]Cook, R. D., Malkus, D. J., Plesha, M. E., and Witt, R. J., *Concepts and Applications of Finite Element Analysis*, 4th ed., Wiley, New York, 2002, pp. 179–201.

[32]Zwillinger, D. (ed.), *CRC Standard Mathematical Tables and Formulae*, CRC Press, Boca Raton, FL, 1996, pp. 360–396.